Performance of the ATLAS Forward Proton Time-of-Flight Detector in 2017

The ATLAS Collaboration

The performance of the ATLAS Forward Proton Time-of-Flight (ToF) detector is studied using the ATLAS LHC data collected in the 2017 running period of LHC Run2. A study of efficiency and time resolution of the ToF is performed. The resolutuion measured in the individual ToF channels ranges between 20 ps to 50 ps, although the efficiency observed is well below 5% in major parts of the analysed calibration stream data. The events from ATLAS physics runs at moderate pile-up of $\mu \sim 2$ taken at the end of 2017 are selected with signals in the ToF stations at both sides of the ATLAS interaction region. The overall time resolution of each ToF detector in these data is found to be 20 ± 4 ps and 26 ± 5 ps for the side A and C side, respectively, where systematic uncertainties dominate the measurement. The difference of the primary vertex z-position measured by ATLAS and the value obtained by the ToFs is also studied. The fits are performed to the distributions yielding resolution of about 6.2 ± 1.0 mm to 8.5 ± 3.4 mm depending on applied data selection which is within uncertainties in agreement with the expectation of 5.5 ± 2.7 mm based on single-channel resolutions.

1 Introduction

A significant fraction of the pp scattering processes proceeds via reactions of type $pp \rightarrow pXp$ (or $pp \rightarrow pX$). There is no colour connection between the secondary system X and the intact leading protons (or proton) in the final state. Therefore, the leading protons carry a large fraction of the initial longitudinal momentum scattered at low angles.

The ATLAS Forward Proton detector (AFP, [1]) is dedicated to the measurement of leading protons' trajectories far from the interaction point. This is possible due to the fact that leading protons deviate from the nominal proton beam to such extent that these deviations can be measured. In the case of the AFP, two stations are located at around 210 m on both sides of the ATLAS interaction region. The AFP detectors are placed in so called Roman Pots (RP) which allow to insert sensitive detectors close to the beam while primary beam-pipe vacuum is preserved. The position of the protons are measured in four layers of a Silicon pixel tracker. The measured positions with respect to the nominal beam protons can then be mapped to the kinematics of the leading proton at the interaction vertex.

The detection of two leading protons in exclusive reactions $pp \rightarrow pXp$ may suffer from background contribution of two independent $pp \rightarrow pX$ processes especially in the high pile-up conditions at the LHC. In order to suppress such background the two outermost AFP stations are equipped with a Time-of-Flight (ToF) detector. By using time difference of arrival times of the leading protons on both A and C sides a constraint is obtained on the expected longitudinal vertex position of the primary $pp \rightarrow pXp$ interaction.

The study of performance of the Time-of-Flight detectors using LHC data from 2017 running period is the subject of the analysis presented in this document. In the first part the evaluation of detection efficiencies and resolutions of time measurement in individual channels of the ToF detector is performed. The second part is devoted to the study of capability of the ToF system to measure the z−coordinate of the vertex position of the primary $pp \rightarrow pXp$ interactions using the times measured in both ToF detectors.

2 AFP and ToF design

The AFP detector consists of four stations located at around 205 m and 217 m denoted as NEAR and FAR, respectively, on (anti)clockwise (A,C) sides of the ATLAS interaction region. Since only the FAR stations are equipped with the ToF detectors only the data from the outermost stations are subject of the study. The AFP tracker is used for reconstruction of tracks pointing to active volumes of ToF providing a selection of suitable events for efficiency and time-resolution measurements. Only a brief account on AFP and ToF design and function is given in this section, for more details see [1].

AFP tracking is provided by a silicon tracker(SiT) consisting of four layers of silicon pixel detectors. The active area covered by the tracking detector is approximately 20×20 mm^2 with a pixel size of 50×250 μm^2. Detectors are tilted by $14°$ providing a spatial resolution design values of $10\,\mu$m and $30\,\mu$m in x and y, respectively, as measured in beam tests [2].

The ToF detectors collect Cherenkov photons created in L-shaped fused silica [3] bars (LQ-bars) which are placed behind the tracker plates. The details on the design of the optical part can be found in [4] and [5] here only a brief account is provided. The geometry of the ToF detector is such that light yield is optimised, given the space constraints of the Roman Pot stations. The LQ-bar consists of two arms: a radiator arm exposed to beam protons and a light guide arm. The two arms are glued together at 90
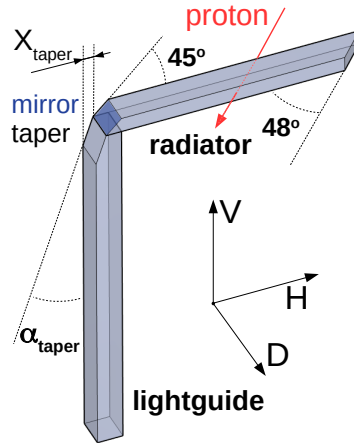
Figure 1: ToF LQ-bar design.

degrees by UV transparent epoxy glue at 90° angle. The elbow presents an Al-mirror and a taper cut to achieve better focusing of the Cherenkov photons, see Figure 1 and Table 1. The photons emitted along the proton trajectory inside the radiator arm propagate to the light-guide arm and to the end of the bars which is attached to the micro-channel plate multi-anode photo-multiplier (MCP-PMT, [6]). The radiator arms are tilted under the Cherenkov angle of 48° with respect to the beam axis which minimises the number of total reflections and leads to optimisation of the time needed for light propagation through the bar. The trailing ends of the radiators are cut parallel to the beam axis in order to reflect downwards emitted photons back to the bar. Four bars are placed one after the other to form a train where there are four trains on each side. The bars and the corresponding channels are denoted as A, B, C, D (or 0 − 3), bar A being the first one to be crossed by protons, bar B the second, etc. Each ToF detector consists of four trains numbered from 0 to 3 as distance from the nominal beam increases. The geometry of the bars is such that the optical path in all bars is equalised. The isochronism of the signals is obtained by adopting bars of decreasing length along the direction of motion of the protons. For a notion of design of the assembled LQ bars and SiT mounted on the Roman Pot flange see Figure 2.

The Cherenkov photon statistics translates to the number of photo-electrons via the quantum efficiency of the PMT's photo-cathode. The number of photo-electrons is amplified by the high voltage applied on the micro-channel plates of the PMTs. The voltage pulses from the PMT anodes are amplified and processed by a constant fraction discriminator (CFD, [7]) providing a square signal for a high performance time-to-digital converter (HPTDC, [8]). The signals are sampled in 1024 bins of about 25 ps in a 25 ns time window which corresponds to the LHC bunch crossing duration. The overall time resolution is influenced by several factors during the formation of the signal in the detector and its read-out in the front-end electronics

3 Single-channel performance analysis

In this section the analysis of single-channel performance is introduced. The definition of data and event samples as well as the methods of efficiency and time resolution extraction are described.

	LQ bar dimensions: $V \times H \times D$ [mm] / α_{taper} [°] / X_{taper} [mm]							
	A bars		B bars		C bars		D bars	
train	radiator	light-guide	radiator	light-guide	radiator	light-guide	radiator	light-guide
0	$2 \times 62.41 \times 6$	$71.3 \times 5 \times 6/18/3$	$2 \times 56.78 \times 6$	$71.3 \times 5 \times 6/18/3$	$2 \times 51.15 \times 6$	$71.3 \times 5 \times 6/18/3$	$2 \times 45.52 \times 6$	$71.3 \times 5 \times 6/18/3$
1	$4 \times 58.16 \times 6$	$67.2 \times 5 \times 6/18/1$	$4 \times 52.53 \times 6$	$67.2 \times 5 \times 6/18/1$	$4 \times 46.9 \times 6$	$67.2 \times 5 \times 6/18/1$	$4 \times 41.27 \times 6$	$67.2 \times 5 \times 6/18/1$
2	$5 \times 52.91 \times 6$	$62.1 \times 5 \times 6/0/0$	$5 \times 47.28 \times 6$	$62.1 \times 5 \times 6/0/0$	$5 \times 41.65 \times 6$	$62.1 \times 5 \times 6/0/0$	$5 \times 36.02 \times 6$	$62.1 \times 5 \times 6/0/0$
3	$5.5 \times 46.6 \times 6$	$56.6 \times 5.5 \times 6/0/0$	$5.5 \times 43.03 \times 6$	$56.6 \times 5.5 \times 6/0/0$	$5.5 \times 35.4 \times 6$	$56.6 \times 5.5 \times 6/0/0$	$5.5 \times 29.77 \times 6$	$56.6 \times 5.5 \times 6/0/0$

Table 1: Table of geometric properties of the LQ-bars. The bars of train 2 and 3 have no taper, indicated with zero values of taper-related values.
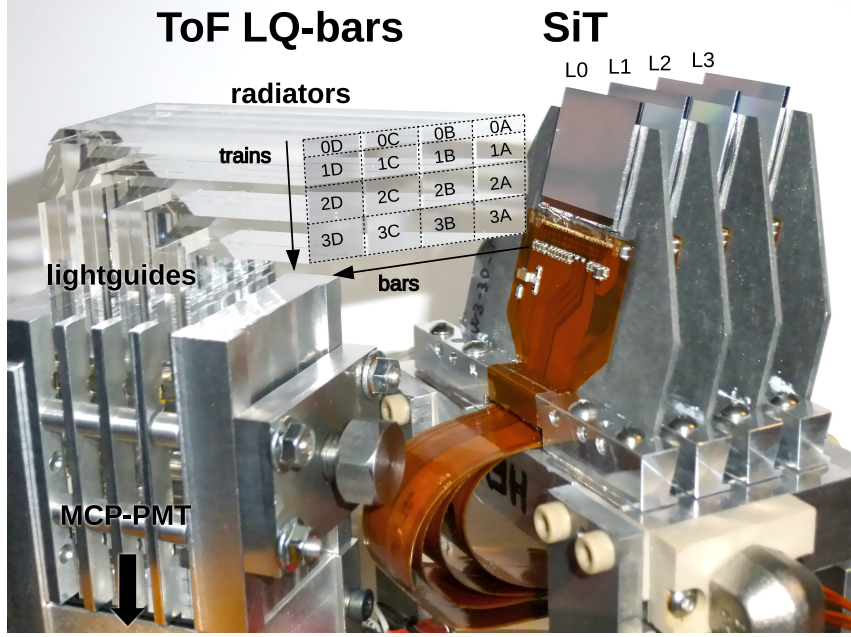

Figure 2: AFP Silicon tracker and ToF LQ-bars.

3.1 Run selection

The presented study was performed with three AFP calibration stream runs only. No attempt was made to correlate the AFP/ToF data with information about collision physics registered by the central ATLAS detector. In Table 2 the list of the analysed runs is given. The ToF PMT operational high voltage was −2 kV in the three runs. The runs 331020 and 336505 taken in low μ conditions are the best for ToF efficiency and time resolution measurement in terms of statistics. The run 336506, although having a lower statistics, is used to study the impact of pile-up effects at high μ on the ToF efficiency. The three runs were acquired with a SiT-track based trigger requiring a track on either of the FAR-A or FAR-C sides of the AFP.

3.2 Event selection

The online event selection is provided by the trigger. The main physics event selection, however, relies on observation of tracks in the SiT. The layout of the pixels on tracker plates is described in terms of row and column numbers corresponding to x and y coordinates, respectively. Due to the rectangular shape of

run #	date	duration [s]	trigger	ToF HV[V]	evt	evt$_{\text{Si-track}}$(FAR-A / FAR-C)
331020	July 29	7504	SiT	-2000	5.7M	1950k / 3047k
336505	Sept 23	12379	SiT	-2000	13.0M	1206k / 6731k
336506	Sept 24	20970	SiT	-2000	0.27M	60k / 45k

Table 2: List of AFP calibration runs recorded in 2017 used for the efficiency and time resolution studies.

the pixels there are 336 rows and 80 columns on each SiT tracker plane. The 14° tilt of the tracker planes means that even a single track parallel to the beam axis may produce two pixel hits in one plane. The selection relies solely on pixel row and column numbers in each plane with. No attempt either to map the pixel positions to a real geometry nor to apply any inter-plane alignment is made since the possible uncertainty on the positions of the SiT components is not expected to be larger than the H-dimension of the LQ-bar (in Table 1). Relying on the crude alignment of the SiT planes the selection criteria applied on the hit pixels ensure signals containing single AFP tracks parallel to the beam axis.

The radiators (trains of radiators) of the ToF LQ-bars are installed in such a way with respect to the SiT that each train covers a limited range of row numbers (x-coordinate) spanning the full range of column numbers (y-coordinate) with respect to the direction parallel to the beam axis. In addition, tracks in narrower ranges of row numbers are used for the analysis to minimise effects related to acceptance deterioration at bar-edges. The row ranges in FAR-A and FAR-C stations are shown in Table 3, they reflect different physical widths of the bars in each train. Also the row ranges are shifted in accordance with different positions of the bars with respect to the SiT in each station. The ranges define safe cores or regions of interest (ROI) from which the tracks point to a single train. Of course, still cross-talk-like signals between certain SiT track core and other than the corresponding train are possible, due to train-to-train Cherenkov photon leakage, PMT channel cross-talk or production of secondary particles. A typical pattern of row versus column number (hitmap) of the selected tracks is shown in Figure 3 for run 331020. The ranges of row numbers defining the core for each train is indicated with a highlighted box.

station	train 0 rows	train 1 rows	train 2 rows	train 3 rows
FAR-A	10 - 30	50-110	130-210	230-320
FAR-C	20 - 40	60-120	140-220	240-330

Table 3: Fiducial cuts on row numbers ensuring the SiT tracks are in geometrical acceptance of the respective ToF trains.

3.3 Measurement of efficiency

The signal from ToF is provided in form of time of proton arrival measured in the corresponding channel in a time window of 25 ns reset by the reference clock. The efficiency of ToF channels are measured by determining fractions of events with any time information in a reference sample of events with SiT tracks, i.e.

$$\varepsilon_{ijk} = \frac{N(\text{bar-ij} \mid \text{track-k})}{N(\text{track-k})}, \tag{1}$$
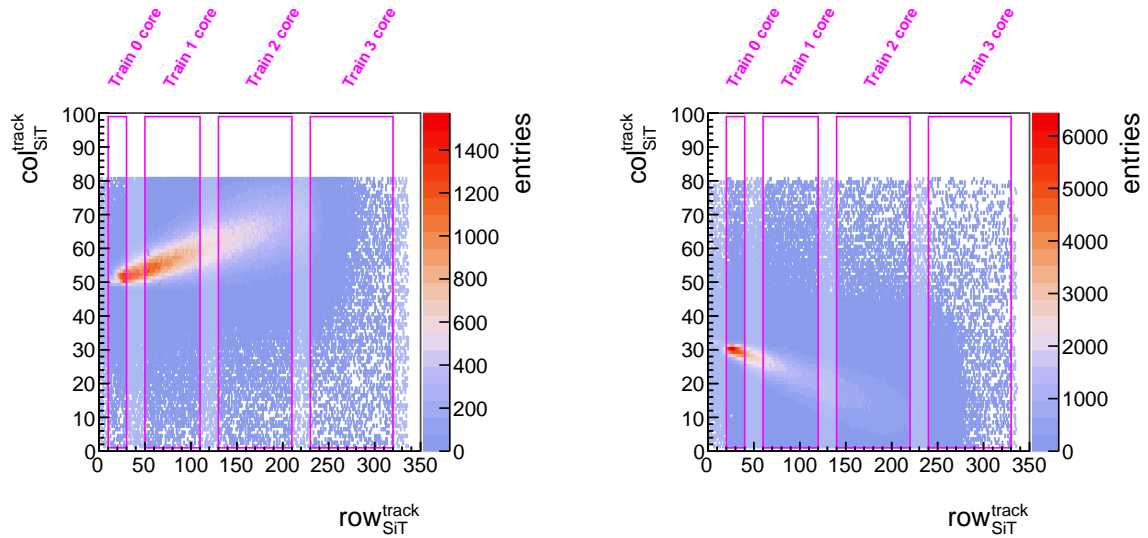
Figure 3: The hitmap of SiT tracks in the FAR A (left Figure) and C (right Figure) stations in run the 331020. Core regions of row numbers of corresponding trains are highlighted. The row and column originally correspond to the SiT pixel numbers with sizes of $50\,\mu$m and $250\,\mu$m, respectively.

where N(bar-ij | track-j) represents number of events with signal in ToF bar-channel i of train number j in the sample containing SiT tracks in train number k. Likewise N(track-k) is the total number of events with SiT track in the train number k. For $j = k$ the efficiency is measured in trains the tracks are pointing to. The efficiency of the whole train is calculated in a straightforward way using events with at least one channel hit in the studied train. It is important to stress that all ToF signal topologies contribute to the efficiency referred as to *any* ToF topology, see top row of Figure 4).
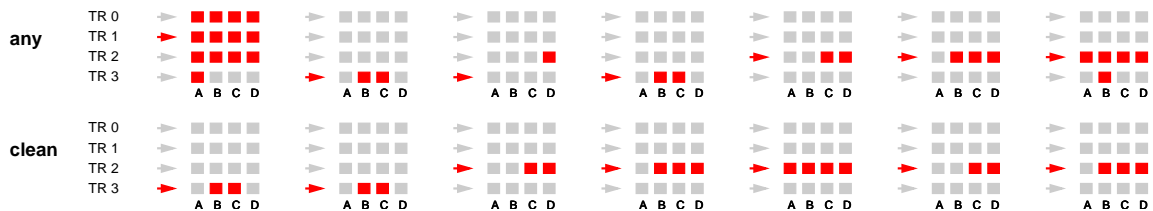

Figure 4: Examples of event topologies. Highlighted arrows and boxes indicate the location of SiT tracks and hit ToF bars. The signal topologies used for efficiency measurement (called any) are shown in the top row. The signal topologies where signal is present in a single ToF train only with an associated SiT track are shown in the bottom row (denoted as clean).

The measured single-channel and combined train efficiencies are presented in Figures 5-7 for all the analysed runs. The top row of Figures corresponds to FAR-A station while the lower row to FAR-C one. Horizontal magenta boxes indicate the train with a reconstructed SiT track. The train efficiencies measured by requiring at least one bar hit in the given train are indicated by vertical magenta lines. A general feature of the applied selection is that with a non-negligible probability signals can be generated also in bars of trains neighbouring the SiT-track train, that is the one the proton track is pointing to. This is can be explained by presence of secondary particles from hadronic showers created in the bars.
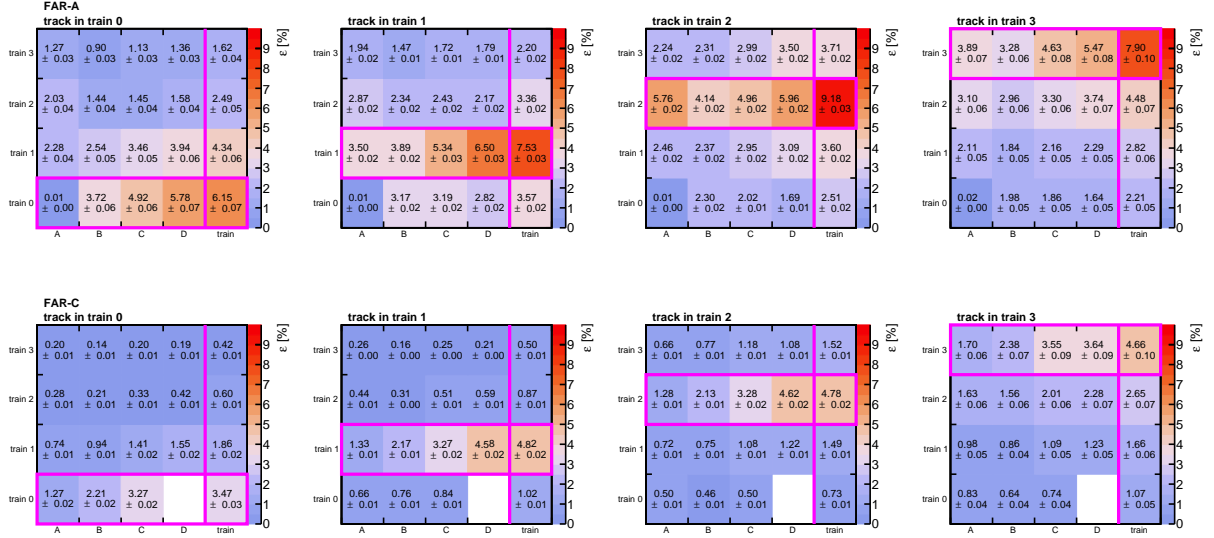
Figure 5: Efficiencies of ToF channels measured in reference samples defined by detection of leading protons in the SiT. The horizontal magenta boxes indicate the 'core' trains with acceptance directly matching that of the SiT track. The vertical magenta boxes indicate the combined efficiency of each train combined over all channels. The efficiencies were obtained from AFP calibration stream run 331020 ($\mu \sim 1$). The top row of plots represents the FAR-A station and the bottom row the FAR-C station.

The efficiencies measured in the SiT-track containing trains vary in ranges of $6 - 9\%$ and $3.5 - 5\%$ in stations FAR-A and FAR-C, respectively, in the run 331020, Figure 5. In the run 336505 (Figure 6) the train efficiencies drop to around 5% and 3% in FAR-A and FAR-C stations, respectively, which may be due to a continuous degradation of the optical part of ToF as well as due to deterioration of the PMT performance as there is a two month gap in between the two runs. The efficiencies measured in the last run 336506 taken at high μ are similar to those measured in run 336505 that was recorded just before the 336506 one, see Figure 7.

In Figure 8 the train efficiencies in events with track in the measured train are shown as a function of time in the runs 331020, 336505 and 336506. Also the μ time dependence is superimposed for comparison. Except for missing data in some parts of the runs no variation of the efficiency correlated with the μ within one run nor with the absolute scale of μ examined in run 336506 is observed.

The efficiencies show a time dependence due to ageing effects while the pileup effects are negligible. The low efficiencies measured in the single channels and the trains are caused by low signal amplitudes at the output of the PMTs. This is caused by the exceeded lifetimes of the PMTs related to the integrated charge generated during the operation.

Figure 6: Efficiencies of ToF channels, presented as for Figure 5, but for calibration stream run 336505 ($\mu \sim 0.05$). The top row of plots represents the FAR-A station and the bottom row the FAR-C station.
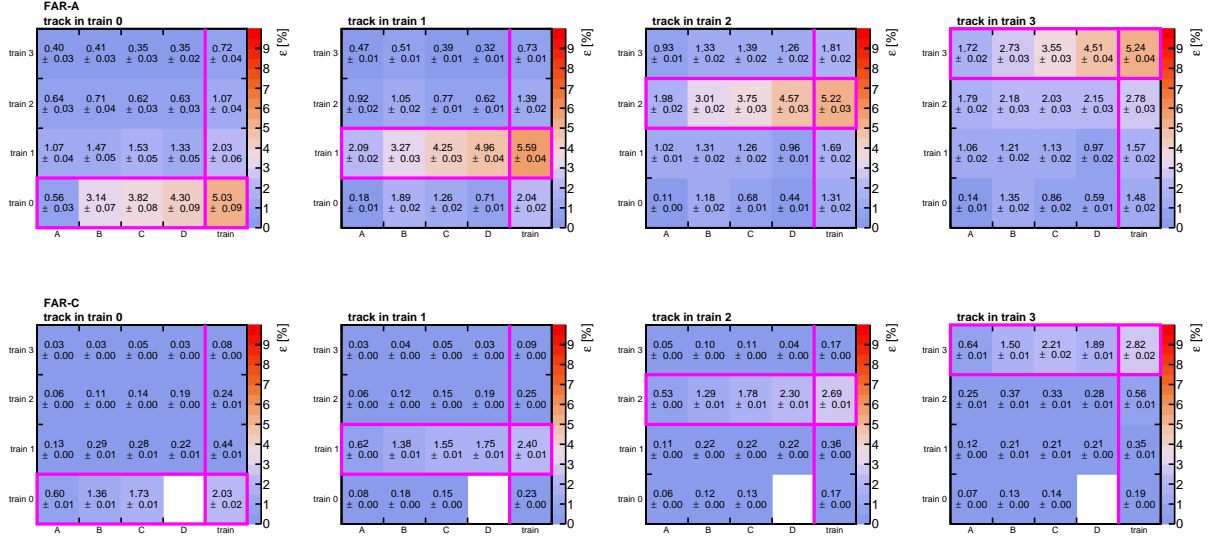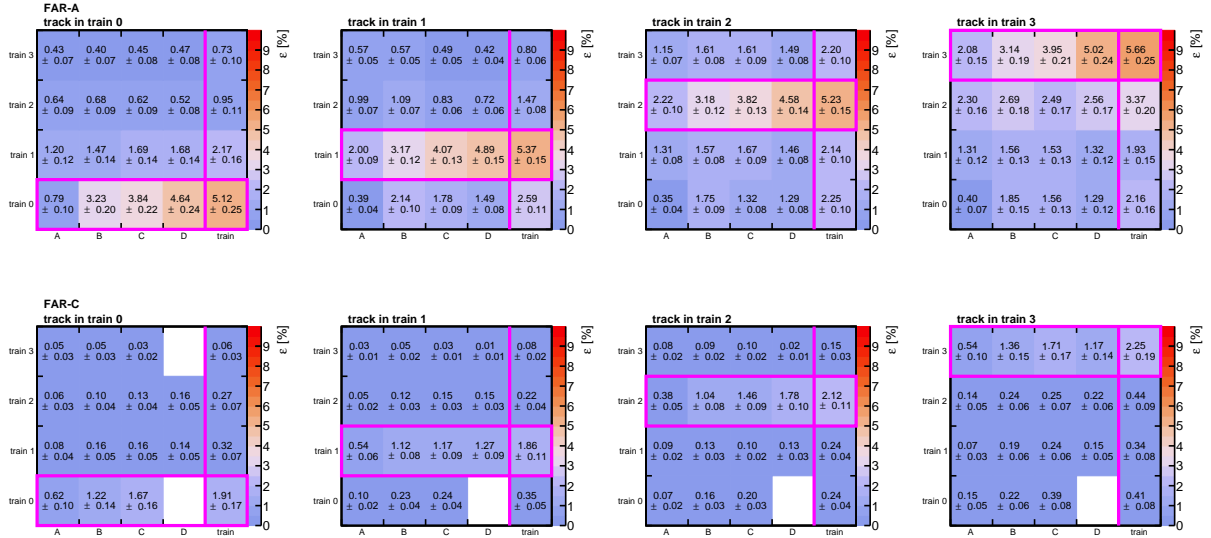
Figure 7: Efficiencies of ToF channels, presented as for Figure 5, but for calibration stream run 336506 ($\mu \sim 30 - 40$). The top row of plots represents the FAR-A station and the bottom row the FAR-C station.
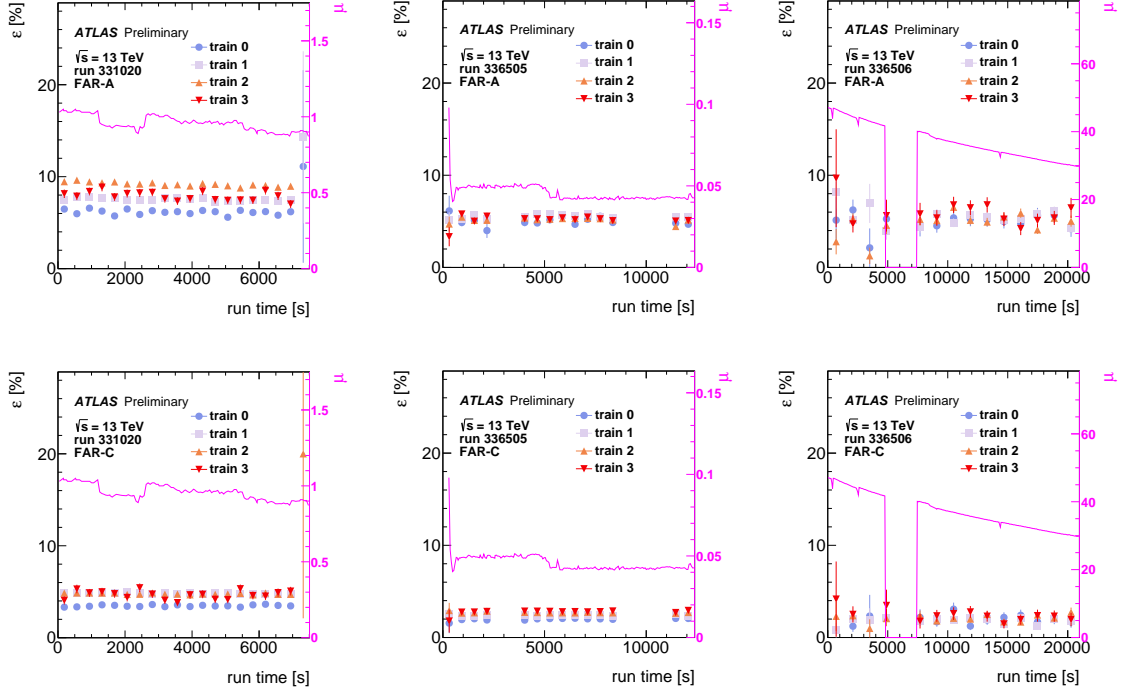
Figure 8: ToF train efficiencies as a function of time in low$-\mu$ AFP calibration stream runs 331020, 336505 and a high$-\mu$ run 336506. The μ time dependence is superimposed as a magenta histogram. The top and bottom rows represent the FAR-A and FAR-C stations, respectively.

3.4 Measurement of time resolution

In this section the method of extraction of resolution in individual channels is explained. The time measured in an i-th ToF channel comprises:

$$t_i = t_{\text{proton}} + t_{i,\text{delay}} + t_{i,\text{smear}} - t_{\text{clock}}, \qquad (2)$$

where t_{proton} represents the proton arrival time whose distribution varies with the size of luminous beam-spot (of order of hundreds of picoseconds), the $t_{i,\text{delay}}$ is a constant channel time offset caused by signal delay in electronics. Unless a hardware change happens, $t_{i,\text{delay}}$ is constant throughout data taking. The $t_{i,\text{smear}}$ represents all random aspects of signal processing such as variation in Cherenkov photon (photo-electron) statistics and effects of electronics. Finally, the t_{clock} represents reference clock signal opening 25 ns window inside which the leading protons from a single bunch-crossing arrive to ToF.

The widths of $t_{i,\text{smear}}$ distributions are subject of the study. In order to eliminate t_{proton} and t_{clock} and to cope with $t_{i,\text{delay}}$, time differences are measured on event by event basis between train channels, i.e. for each train one has

$$\Delta t_{ij} = t_i - t_j = t_{i,\text{delay}} - t_{j,\text{delay}} + t_{i,\text{smear}} - t_{j,\text{smear}}. \qquad (3)$$

There are six unique Δt_{ij} combinations in the case of four ToF channels. Only events with topologies where at least two hits are required in one and only ToF train (*clean*), see bottom row of Figure 4, are considered for the resolution determination. The clean selection ensures the Δt_{ij} shapes are well described

9

by Gaussian fits. The presence of t_{delay} causes the Δt_{ij} distributions peak at non-zero values in general. The fitted widths of the Δt_{ij} distributions, σ_{ij}, are used for extraction of individual channel resolutions $\sigma_i = \sqrt{Var(t_{i,\text{smear}})}$. By evaluation of $E[(t_i - t_j)^2]$ and assuming $t_{i,\text{delay}}$ has zero variance one obtains

$$\sigma_{ij}^2 = Var(t_{i,\text{smear}} - t_{j,\text{smear}}) = \sigma_i^2 + \sigma_j^2 - 2\rho_{ij}\sigma_i\sigma_j, \tag{4}$$

where ρ_{ij} is a correlation between pairs of $t_{i,\text{smear}}$ and $t_{j,\text{smear}}$. Due to the fact that a true or reference t_{proton} is unknown and it varies significantly it is impossible to extract the correlation factor ρ_{ij} from single pairs of t_i and t_j times measured in the real data. An attempt was made to extract the correlations from pairs of time differences sharing the third time as reference, i.e. Δt_{ik} and Δt_{jk} for ρ_{ij}. This method was found not to be conclusive since non-Gaussian tails and insufficient data statistics complicate the extraction. In reality the correlation of times measured in adjacent channels are introduced by charge sharing between PMT pixels leading to modification pulse shapes. In beam tests[9] it was found that the charge induced on PMT pixels coming from neighbouring pixels was found to contribute by about 10% A conservative approach is adopted here assuming a global variation of correlation factors between all channels of ±0.2 and 0 which is supported by statistical analysis of the data described in the next paragraph.

The six equations $\sigma_{ij} = \sqrt{\sigma_i^2 + \sigma_j^2 - 2\rho_{ij}\sigma_i\sigma_j}$ represent an over-determined system. The σ_{ij} values constrain the possible space of σ_i and σ_j which are obtained by minimising the expression

$$\Sigma_{ij} \frac{\left(\sigma_{ij} - \sqrt{\sigma_i^2 + \sigma_j^2 - 2\rho_{ij}\sigma_i\sigma_j}\right)^2}{\left(\delta_{\text{fit}}(\sigma_{ij})\right)^2}, \tag{5}$$

where $\delta_{\text{fit}}(\sigma_{ij})$ is statistical uncertainty of the fitted value of σ_{ij}. As mentioned earlier correlations between times measured in each channel are varied by ±0.2 around nominal value of zero. These values are also consistent with values obtained from fits where ρ_{ij} are considered as free fit parameters. The fits in this case are performed over a combined dataset of six binned Δt_{ij} distributions in ranges where signals are described by Gaussian shapes. The variations of fitted ρ_{ij} are safely covered by a ±0.2 band. The differences between the results using $\rho_{ij} = 0$ and $\rho_{ij} = \pm0.2$ are interpreted as a systematic uncertainty.

Another source of uncertainty resides in a non-linear response of the HPTDC to input time. The HPTDC may suffer from irregularities effectively changing the widths of the 1024 bins which in turn results in an artificial preference of times measured in wider bins and also in shifts of the measured time information. The calibration parameters are known for one particular ToF channel only, yet it can be expected that the parameters do not vary much between channels. The full set of calibrations for all channels is not available. Nonetheless, it can be expected that the HPTDC non-linearity effects smear out if one is interested in widths of the time differences Δt_{ij} measured in channels of one train. This was confirmed both by using the single channel calibration for all channels and also by making an attempt to deduce the individual HPTDC's channel bin widths from the real data. The effect of these two approaches on the widths of the Δt_{ij} distributions was estimated to change the widths by ±5 ps at most if compared with uncalibrated results. Therefore, the ±5 ps variation of the σ_{ij} values extracted from the uncalibrated times is used as a very conservative value to account for the systematic uncertainty on the HPTDC calibration.

The single channel resolutions for the clean ToF hit topology are presented in Figure 9 and in Tables 4 and 5 for the runs 331020 and 336505. Due to the LQ-bar design and also verified by simulations it is known that photon leakage occurs between the LQ-bars downstream the proton motion, leading to a gradual photon enrichment of the latter bars. The worst resolutions of $40 - 50$ ps are observed in the A channels of the trains which have lowest photon yield. The following bars gradually profit from the photon
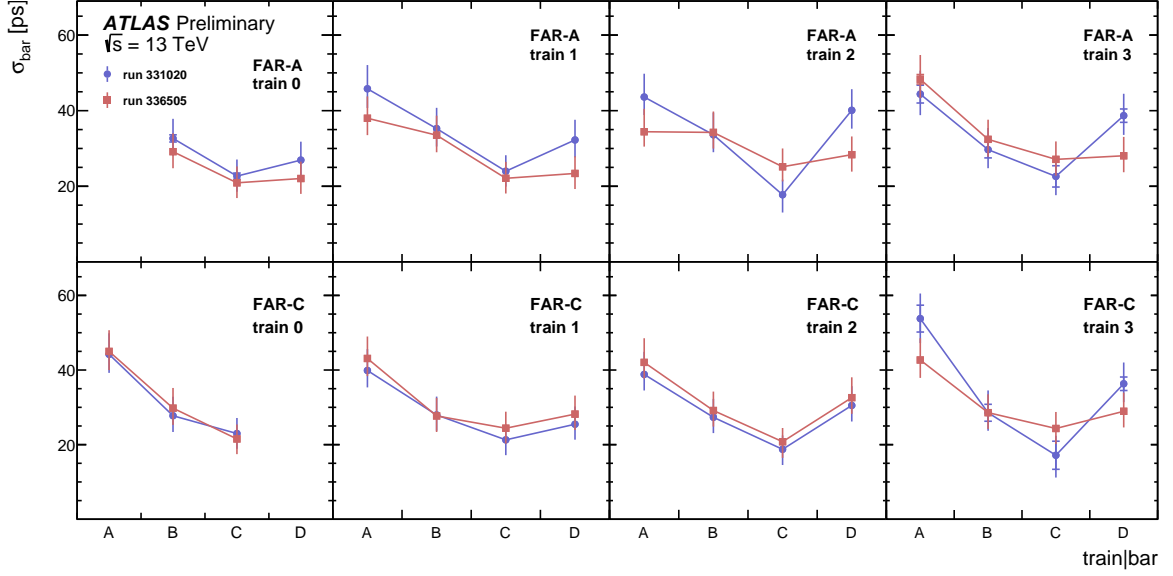
Figure 9: Time resolutions measured in runs 331020 (circles) and 336505 (squares). The size of full error bars indicates the statistical and systematic uncertainty added in quadrature for each point. The inner error bars represent the statistical uncertainty only.

enrichment yielding resolutions of $30 - 20$ ps of the B and C channels. Despite the photon enrichment from the previous bars, the resolution measured in the D channel is systematically worse in all trains. The effect can be explained by lower signal amplitude of the last train channels as the charge sharing between channels is weaker for the D channel. The same effect worsens the resolutions in the A channels. The total uncertainty of the measured resolutions reaches 6 ps at most and is composed of statistical uncertainty stemming from the minimisation procedure applied to equation 5 and of systematic uncertainties from ρ_{ij} and σ_{ij} variations by ± 0.2 and ± 5 ps as described above in this section. The systematic uncertainties dominate in all channels.

	station	train#	σ_A [ps]	σ_B [ps]	σ_C [ps]	σ_D [ps]
RUN 331020	FAR-A	0	N/A	33 ± 1 (stat) $^{+5}_{-4}$ (syst)	23 ± 1 (stat) $^{+4}_{-4}$ (syst)	27 ± 1 (stat) $^{+5}_{-4}$ (syst)
		1	46 ± 1 (stat) $^{+6}_{-5}$ (syst)	35 ± 0 (stat) $^{+5}_{-5}$ (syst)	24 ± 1 (stat) $^{+4}_{-4}$ (syst)	32 ± 0 (stat) $^{+5}_{-5}$ (syst)
		2	44 ± 1 (stat) $^{+6}_{-5}$ (syst)	34 ± 0 (stat) $^{+6}_{-5}$ (syst)	18 ± 1 (stat) $^{+4}_{-5}$ (syst)	40 ± 0 (stat) $^{+6}_{-5}$ (syst)
		3	44 ± 2 (stat) $^{+6}_{-5}$ (syst)	30 ± 2 (stat) $^{+5}_{-4}$ (syst)	23 ± 3 (stat) $^{+4}_{-4}$ (syst)	39 ± 2 (stat) $^{+6}_{-5}$ (syst)
	FAR-C	0	44 ± 1 (stat) $^{+6}_{-5}$ (syst)	28 ± 0 (stat) $^{+5}_{-4}$ (syst)	23 ± 0 (stat) $^{+4}_{-4}$ (syst)	N/A
		1	40 ± 0 (stat) $^{+6}_{-5}$ (syst)	28 ± 0 (stat) $^{+5}_{-4}$ (syst)	21 ± 0 (stat) $^{+4}_{-4}$ (syst)	25 ± 0 (stat) $^{+5}_{-4}$ (syst)
		2	39 ± 0 (stat) $^{+6}_{-4}$ (syst)	27 ± 0 (stat) $^{+5}_{-4}$ (syst)	19 ± 0 (stat) $^{+4}_{-4}$ (syst)	31 ± 0 (stat) $^{+5}_{-4}$ (syst)
		3	54 ± 4 (stat) $^{+6}_{-5}$ (syst)	29 ± 2 (stat) $^{+6}_{-4}$ (syst)	17 ± 4 (stat) $^{+4}_{-5}$ (syst)	36 ± 2 (stat) $^{+5}_{-5}$ (syst)

Table 4: Single bar resolutions measured in run 331020.

station	train#	σ_A [ps]	σ_B [ps]	σ_C [ps]	σ_D [ps]
FAR-A	0	N/A	29± 1 (stat) $^{+5}_{-4}$ (syst)	21± 1 (stat) $^{+4}_{-4}$ (syst)	22± 1 (stat) $^{+4}_{-4}$ (syst)
	1	38± 1 (stat) $^{+6}_{-4}$ (syst)	34± 0 (stat) $^{+5}_{-5}$ (syst)	22± 0 (stat) $^{+4}_{-4}$ (syst)	23± 0 (stat) $^{+5}_{-4}$ (syst)
	2	34± 1 (stat) $^{+5}_{-4}$ (syst)	34± 0 (stat) $^{+6}_{-4}$ (syst)	25± 0 (stat) $^{+5}_{-5}$ (syst)	28± 0 (stat) $^{+5}_{-4}$ (syst)
	3	48± 1 (stat) $^{+6}_{-5}$ (syst)	32± 1 (stat) $^{+5}_{-5}$ (syst)	27± 1 (stat) $^{+5}_{-5}$ (syst)	28± 1 (stat) $^{+5}_{-4}$ (syst)
FAR-C	0	45± 0 (stat) $^{+6}_{-5}$ (syst)	30± 0 (stat) $^{+5}_{-4}$ (syst)	22± 0 (stat) $^{+4}_{-4}$ (syst)	N/A
	1	43± 0 (stat) $^{+6}_{-5}$ (syst)	28± 0 (stat) $^{+5}_{-4}$ (syst)	24± 0 (stat) $^{+4}_{-4}$ (syst)	28± 0 (stat) $^{+5}_{-4}$ (syst)
	2	42± 0 (stat) $^{+6}_{-4}$ (syst)	29± 0 (stat) $^{+5}_{-4}$ (syst)	21± 0 (stat) $^{+4}_{-4}$ (syst)	33± 0 (stat) $^{+5}_{-4}$ (syst)
	3	43± 0 (stat) $^{+6}_{-5}$ (syst)	29± 0 (stat) $^{+5}_{-4}$ (syst)	24± 0 (stat) $^{+4}_{-4}$ (syst)	29± 0 (stat) $^{+5}_{-4}$ (syst)

RUN 336505

Table 5: Single bar resolutions measured in run 336505.

4 Vertex matching analysis

In this section the analysis of capability of the ToF system to measure the $z-$coordinate of the primary vertex of the $pp \rightarrow pXp$ interactions is introduced.

The principle of the vertex reconstruction relies on the measurement of the proton arrival times by ToF on both A and C sides given by

$$z_{\text{ToF}} = \frac{c}{2}(t_{FAR-C} - t_{FAR-A}), \qquad (6)$$

where the positive $z-$axis points in the A-side direction and it is assumed that the ToF stations are located at equal distances from the origin of the coordinate system and z_{ToF} indicates that the value is obtained from the ToF measurement. In the real conditions calibration corrections for offsets in the position of ToF stations, trains and time delays of individual channels must be performed.

The resolution of the z_{ToF} can be evaluated by measuring distribution of $z_{\text{ATLAS}} - z_{\text{ToF}}$, where z_{ATLAS} is the value of the reconstructed primary vertex $z-$position provided the central ATLAS detector. The width of the distribution reflects the combined resolution of the z_{ToF} and z_{ATLAS} measurement. If pile-up interactions are present the distribution of $z_{\text{ATLAS}} - z_{\text{ToF}}$ contains also the background contribution from random coincidences of protons measured in ToF not originating from $pp \rightarrow pXp$ processes and whose arrival time spreads are driven by the beamspot size.

4.1 Run and event selection

The best conditions for vertex matching analysis would be provided by data from low-μ runs. The statistics of events with ToF signal is limited by the low integrated luminosity of the low-μ runs and by the small detection efficiency of the ToF. Therefore, a run with $\langle\mu\rangle \sim 2$ is selected from the end of 2017 LHC data taking period (Run 341419). The AFP triggers used in this run contain the SiT based `L1AFP_A_OR_C` condition. There are also about ~ 2 M potential jet events provided by the `HLT_j20_L1AFP_A_OR_C` trigger. A slightly lower high voltage of -1950 kV is applied on the ToF PMTs in this run. The SiT triggers ensure higher probability of registering ToF signals on the corresponding FAR side. In order to increase the useful yield of ToF events as much as possible, the selection criteria on the SiT tracks are totally relaxed on both sides. The final event selection condition applied on either side of the ToF independently requires that the ToF signal is present exclusively in one train only with at least one channel hit in the train. The events passing the ToF selection on one side only are called single-tag whereas double-tag events pass the criteria on both sides.
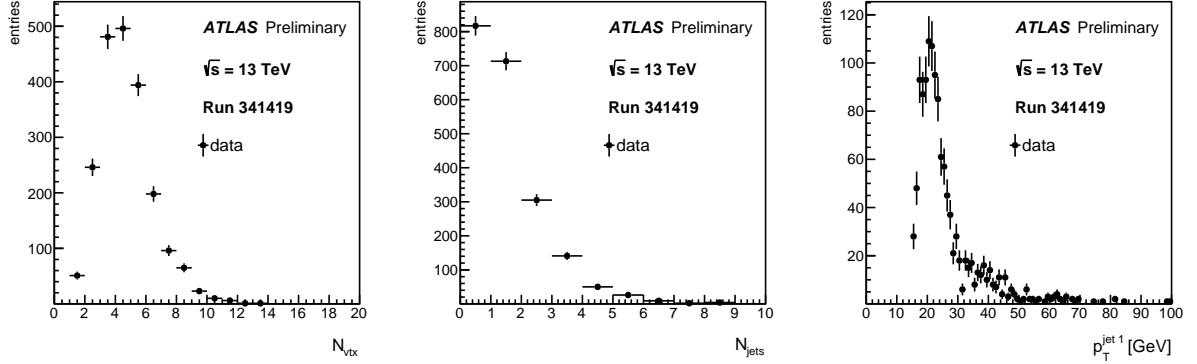
12

Figure 10: The distributions of number of vertices, N_{vtx}, number of reconstructed jets, N_{jets}, and the transverse momentum of the leading jet $p_{\text{T}}^{\text{jet 1}}$ in the run 341419.

The control distributions of number of vertices reconstructed by ATLAS, N_{vtx}, number of reconstructed jets, N_{jets}, and the transverse momentum of the leading jet $p_{\text{T}}^{\text{jet 1}}$ obtained in run 341419 are shown in Figure 10. The pre-selection of the data requiring that the events contain ToF signal on either side biases the mean value of reconstructed number of vertices from the expected $\langle \mu \rangle = 2$ to a higher value of around 4. This is not surprising, since the probability of registering signals in ToF increases with higher number of interactions taking place during one bunch-crossing.

4.2 Time resolutions of trains and stations

The single-channel ToF resolutions are measured in the run 341419 using the method of extraction identical to the one used in Section 3.4. The resolutions provide the input for estimation of the expected time resolution of the individual stations as well as the combined resolution of both stations for the measurement of primary vertex z-position with ToF. The distribution of all possible signal patterns that can occur in a single train of four channels, i.e. 16 combinations, are used to calculate a weighted average over the observed ToF (ABCD) hit patterns.

4.3 Corrections of time delays

4.3.1 Channel time delays

The time measured by a single ToF train is obtained as an average of the single-channel times. In order to make the calculation of the train time sensible no matter the number of contributing channels one needs to correct for the constant time delay contribution, $t_{i,\text{delay}}$, in each channel, see (2). This can be done by studying distributions of differences of the channel times Δt_{ij} defined in (3). The mean value of the time difference distribution of channels i and j of a single train reads

$$\langle \Delta t_{ij} \rangle = \langle t_{i,\text{smear}} + t_{i,\text{delay}} - t_{j,\text{smear}} - t_{j,\text{delay}} \rangle = t_{i,\text{delay}} - t_{j,\text{delay}} \tag{7}$$

13

where the fact that for all channels $\langle t_{i,\text{smear}} \rangle = 0$ is used. Using the values of $\langle \Delta t_{ij} \rangle$ obtained from Gaussian fits the time delays can be estimated by minimisation of

$$\Sigma_{ij} \frac{\left(\Delta t_{ij} - \left(t_{i,\text{delay}} - t_{j,\text{delay}}\right)\right)^2}{\left(\delta_{\text{fit}}(\Delta t_{ij})\right)^2}, \tag{8}$$

against the $t_{i,\text{delay}}$ for all channels in a given train. The solution can be found up to an additive constant. Therefore, a fixing condition of $t_{B,\text{delay}} = 500$ ps is used in all trains of both ToF stations and is only a matter of convenience. The extracted $t_{i,\text{delay}}$ values are summarised in Table 6 for the run 341419 where the statistical precision of their determination is better than 1 ps.

RUN 341419

station	train#	$t_{A,\text{delay}}$ [ps]	$t_{B,\text{delay}}$ [ps]	$t_{C,\text{delay}}$ [ps]	$t_{D,\text{delay}}$ [ps]
FAR-A	0	N/A	500	66	470
	1	775	500	766	989
	2	862	500	192	796
	3	445	500	64	115
FAR-C	0	1078	500	723	N/A
	1	965	500	772	683
	2	515	500	497	667
	3	371	500	369	91

Table 6: Single-channel time delay constants $t_{i,\text{delay}}$ measured in run 341419. Statistical errors are below 1 and 0.1 ps for FAR-A and FAR-C stations respectively.

4.3.2 y-correction

The assumption of constant nature of $t_{i,\text{delay}}$ values is actually only approximate. There is a geometrical effect not fully examined in this analysis due to the limited statistics of the data. The design and positioning of the LQ-bars causes a dependence of the measured channel time on the position the incident proton enters the LQ-bar radiator along the V-direction (in Figure 1) or the $y-$direction in the ATLAS coordinate system. Protons hitting the radiator tip will produce photons travelling with the speed c/n inside the radiator volume which is slant under 48° producing a delayed signal compared to protons hitting the radiator close to the LQ-bar elbow. The protons pointing to the LQ-bar elbow although travelling an extra distance of about 2 cm in vacuum produce a Cherenkov photon signal reaching the PMT earlier. Assuming the index of refraction of 1.5 the slope of the correction (y-correction), linear in y, is estimated to be equal to ~ 3.75 ps/mm. No evaluation of systematic uncertainties of the $y-$correction slope either by variation of the chosen value of refraction index or by a direct extraction of the measured time dependence on the y_{track} was done. In order to be able to apply the y-correction, the information about the position of the incident track measured in SiT needs to be known. Unfortunately, introducing cuts on SiT tracks on top of the ToF selection reduces statistics to such level that the analysis outcomes are not very conclusive. Instead, the additional smearing of the measured times is estimated by error propagation of the y-correction using the standard deviation of distributions of y-coordinate values of the local tracks obtained from events with ToF cuts relaxed. The smearing is determined for every train of both ToF stations and is added in quadratures as an uncertainty to the time resolution of trains obtained from the single-channel time resolutions.

14

4.3.3 Train time delays

The train times obtained by averaging the time-delay-corrected channel times are yet not comparable between each other within one station due to the ad-hoc choice of $t_{B,\text{delay}} = 500$ ps. Also the train times will inherently feature shifts introduced by the geometrical effect discussed in the previous section which is assumed to contribute approximately linearly as a function of the train number. Therefore for each train there is a time shift that needs to be determined leading to possibility to define the station time irrespectively of the actual train the signal is observed in a particular event. Such shifts can be extracted from distributions of differences of train times - now measured independently in the FAR-A and FAR-C stations. The distributions of differences of the train times and consequently of z_{ToF} by using (6) can be with convenience evaluated not only on the event-by-event basis but also from the whole data sample combining non-related events (event mixing, ME). The event mixing is utilised in such a way that the number of randomly combined events is limited to a value where the probability of using one combination more than once is kept below one per mille. Also, in order to eliminate a possible bias and ensure the independence from the eventual analysis of ToF double tag events, the double tag events are rejected in filling the time buffers used for event mixing. Only the events from a single lumiblock are used for the mixing because the beamspot z−position, z_{BS}, is known per lumiblock in the ATLAS data. It is also assumed that z_{BS} does not vary significantly within one lumiblock. In the ideal case of a calibrated ToF system the mean value of the z_{ToF} from mixed events should reproduce the z_{BS} dependence on the lumiblock number. The calibration procedure amounts to determination of eight shifts s_A^i and s_C^j associated with trains i and j in stations FAR-A and FAR-C. Set of 16 equations is studied

$$\langle \sum_{LB} z_{\text{ToF}}^{(ij)} - z_{\text{BS}} \rangle = s_A^i - s_C^j, \tag{9}$$

where the ij indices in $z_{\text{ToF}}^{(ij)}$ refer to train numbers in the FAR-A and FAR-C stations, respectively. The sum over lumiblocks, $\sum_{LB}$, stresses the fact that within a given lumiblock the sample of mixed events uses a constant z_{BS} value to correct for possible z_{BS} changes. These equations represent conditions that can be solved for s_A^i and s_C^j in the same manner as in (8) up to an additive constant which also covers an imprecision in knowledge of the exact physical distance between the ToF stations. In order to cope with the freedom in the choice of the constant term, the value of s_A^0 is set to zero. The extracted shifts for run 341419 are summarised in Table 7. By subtracting these correction factors from the train times in each station the difference of station times and consequently the distribution of z_{ToF} (or $z_{\text{ToF}}^{\text{ME}}$ from the mixed event sample) can be studied and compared with the z_{BS} as a function of lumiblock. In Figure 11 an evidence of sensitivity of ToF to z_{BS} variations is provided. On the left side of Figure 11 the distribution of $z_{\text{ToF}}^{\text{ME}}$ as a function of lumiblock is shown. The distributions are fitted with a Gaussian function in every lumiblock slice and the mean values $\langle z_{\text{ToF}}^{\text{ME}} \rangle$ are compared with the z_{BS} provided by ATLAS. On the right side of Figure 11 the distribution of $z_{\text{BS}} - \langle z_{\text{ToF}}^{\text{ME}} \rangle$, over all lumiblocks is shown. The corrections factors s_A^i, s_C^j perform well as the distribution is reasonably centred around zero with standard deviation of about four millimetres.
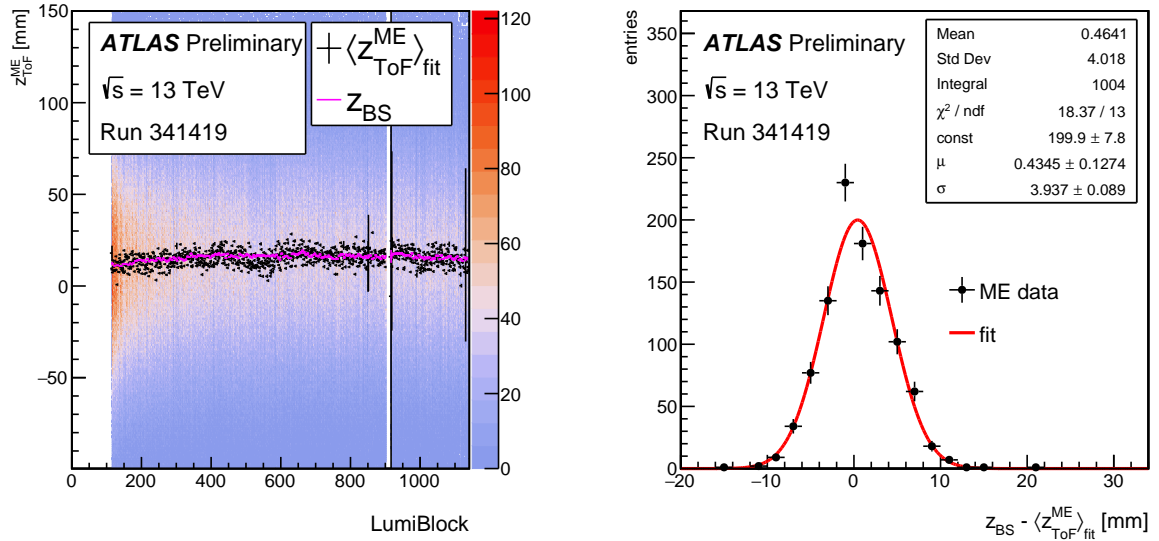
Figure 11: The left figure shows the distribution of $z_{\mathrm{ToF}}^{\mathrm{ME}}$ from mixed event sample as a function of lumiblock number of the run 341419. The mean values, $\langle z_{\mathrm{ToF}}^{\mathrm{ME}} \rangle$, obtained from Gaussian fits are shown as a black histogram. The z_{BS} values provided by ATLAS are represented by the magenta histogram. The right figure quantifies the distribution of the $\langle z_{\mathrm{ToF}}^{\mathrm{ME}} \rangle$ values around the z_{BS} from all lumiblocks of the run 341419.

RUN 341419

station	train 0	train 1	train 2	train 3
FAR-A	0.0 mm	106.8± 0.2 mm	60.7± 0.2 mm	50.2± 0.2 mm
FAR-C	379.4± 0.1 mm	428.9± 0.2 mm	395.1± 0.2 mm	342.5± 0.2 mm

Table 7: Train shifts $s_{\mathrm{station}}^{\mathrm{train}}$ measured in run 341419. The shift in train 0 of the FAR-A station is set to zero since the time shifts are well defined up to a constant factor.

4.4 Results

The vertex matching analysis is performed using a ToF double-tagged data sample, i.e. events with signals measured exclusively in a single train in both ToF stations. Shapes of the $z_{\mathrm{ATLAS}} - z_{\mathrm{ToF}}$ distributions, where z_{ATLAS} is the primary vertex position measured by ATLAS and the z_{ToF} values are obtained from station times defined in Section 4.3, are used to estimate the vertex resolution reached by the ToF detectors. The fits to the distributions are performed using a double-Gaussian p.d.f. accounting for the signal and background components. The mean value and width of the background component of the p.d.f. is fixed from a previous Gaussian fit to the $z_{\mathrm{ATLAS}} - z_{\mathrm{ToF}}$ distribution where the z_{ATLAS} and the station times used for z_{ToF} calculation are taken from previously filled event buffers, i.e. mimicking the combinatorial effects. The mean value of the signal component is fixed to the same value as used for the background one. The fits are performed to an unbinned datasample using the extended negative log-likelihood approach as implemented in RooFit [10] within ROOT [11].

The baseline for the ToF resolution is given by the time resolution of the single-channels. In Figure 12 the resolutions for single-train hit patterns measured in 341419 are shown. The resolutions of the single-channel resolutions in the run 341419 are comparable to those observed in runs 331020 and 336505. The
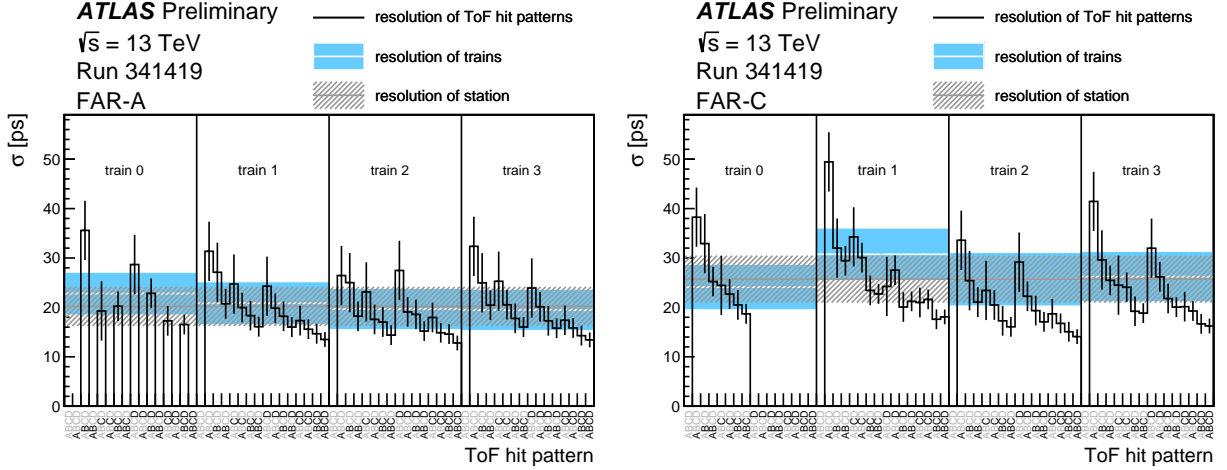
Figure 12: The resolutions of the ToF, in run 341419, for all observed signal patterns shown as a simple histogram where the hit channels are highlighted in the ABCD sequence of channels. The resolutions of trains are indicated by the white line histogram with blue error band. The station resolutions are visualised by a hatched histogram.

effect of averaging can be observed for the hit patterns with higher multiplicity where the resolutions improve to levels below 20 ps for the fully occupied trains. In the selected data set channels (A, FAR-A, train 0) and (D, FAR-C, train 0) were not operational. Based on the analysis of runs 331020 and 336505, the single-channel systematic uncertainty is set to 6 ps. The measured train resolutions vary between 20 ps and 30 ps with typical uncertainty of about $4 - 5$ ps. The station resolutions obtained as weighted average of the train resolutions over the number of events observed in the trains yield

$$\sigma_{\text{FAR-A}}^{\text{ToF}} = 20.2 \pm 4.0 \text{ ps} \quad \sigma_{\text{FAR-C}}^{\text{ToF}} = 25.7 \pm 4.7 \text{ ps}, \tag{10}$$

By using equation (6), the spatial resolution in the z-coordinate results:

$$\sigma_{\text{expected}}^{\text{channels}}(\Delta z) = 4.9 \pm 0.7 \text{ mm}. \tag{11}$$

The resolutions are measured by comparing the same proton arrival times measured in channels of a particular train in a single event, therefore independently of the y-position of the incident proton track. The additional smearing due to the y-position of the incoming protons is evaluated by propagation of the widths of the track y-coordinate distributions obtained beforehand (shown in Figure 13) through the linear dependence of the correction, i.e. $\delta_{\text{y-corr}}$ [ps] $= 3.75$ [ps/mm] $\times \delta(y_{\text{track}})$ [mm], where the slope parameter and the standard deviation of y_{track} distributions $\delta(y_{\text{track}})$ are measured in ps/mm and mm, respectively. The final expected resolutions of the ToF accounting also on the smearing due to the unknown y-coordinate of the incident proton tracks reads

$$\sigma_{\text{expected}}^{\text{ToF}}(\Delta z) = 5.5 \pm 2.7 \text{ mm}, \tag{12}$$

where the uncertainty is obtained by adding the statistical of (11) and y-dependent uncertainties in quadratures. The $y-$dependent uncertainty is estimated from maximum deviation of the ToF resolution introduced by individual shifts of the station resolutions (10).
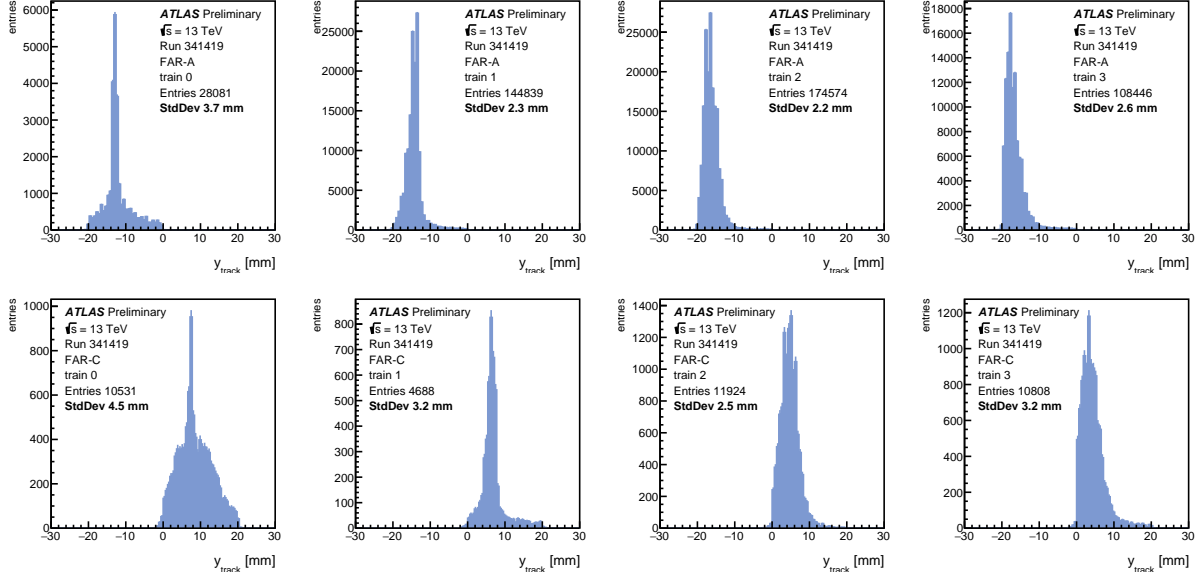
Figure 13: The distributions of y-positions of tracks measured for all trains of both ToF stations in run 341419. The assignment of the tracks to trains is made by using previously defined fiducial cuts in the x-coordinate that provide mapping of the geometrical acceptance of ToF trains to the SiT.

In Figure 14 the distributions of $z_{\text{ATLAS}} - z_{\text{ToF}}$ are presented in three cut scenarios with respect to number of vertices reconstructed by ATLAS, no N_{vtx} cut, $N_{\text{vtx}} \leq 5$, $N_{\text{vtx}} \leq 4$ and $N_{\text{vtx}} \leq 3$, respectively. The data excess around $z_{\text{ATLAS}} - z_{\text{ToF}} = 0$, within the large errors, is not incompatible with contribution of double-Pomeron exchange (DPE) processes [12–14], where varying momentum fractions of the Pomerons enter the hard process. Since the data do not contain final states with high enough hard scale the most part of the initial collision energy of the Pomerons must be present in form of Pomeron remnants. The extracted signal and background parameters as well as the expected resolution are summarised in Table 8. The signal widths vary between about 6 mm to 9 mm with non-negligible statistical uncertainties suggesting sensitivity of the fits to statistics of the available data. The results are nevertheless in agreement with the expected resolution of the ToF detector, 5.5 ± 2.7 mm. The dependence of the fitted number of signal events decreases slower than the number background events if the cut value on the number of vertices decreases as one would expect.

RUN 341419

	no N_{vtx} cut	$N_{\text{vtx}} \leq 5$	$N_{\text{vtx}} \leq 4$	$N_{\text{vtx}} \leq 3$
σ_{sig}	6.2 ± 1.0 mm	7.9 ± 3.0 mm	8.1 ± 1.3 mm	8.5 ± 3.4 mm
n_{sig}	67 ± 12	58 ± 13	61 ± 11	38 ± 10
n_{bgd}	1950 ± 25	1559 ± 23	1162 ± 20	689 ± 16
$\sigma_{\text{expected}}^{\text{ToF}}$	5.5 ± 2.7 mm			

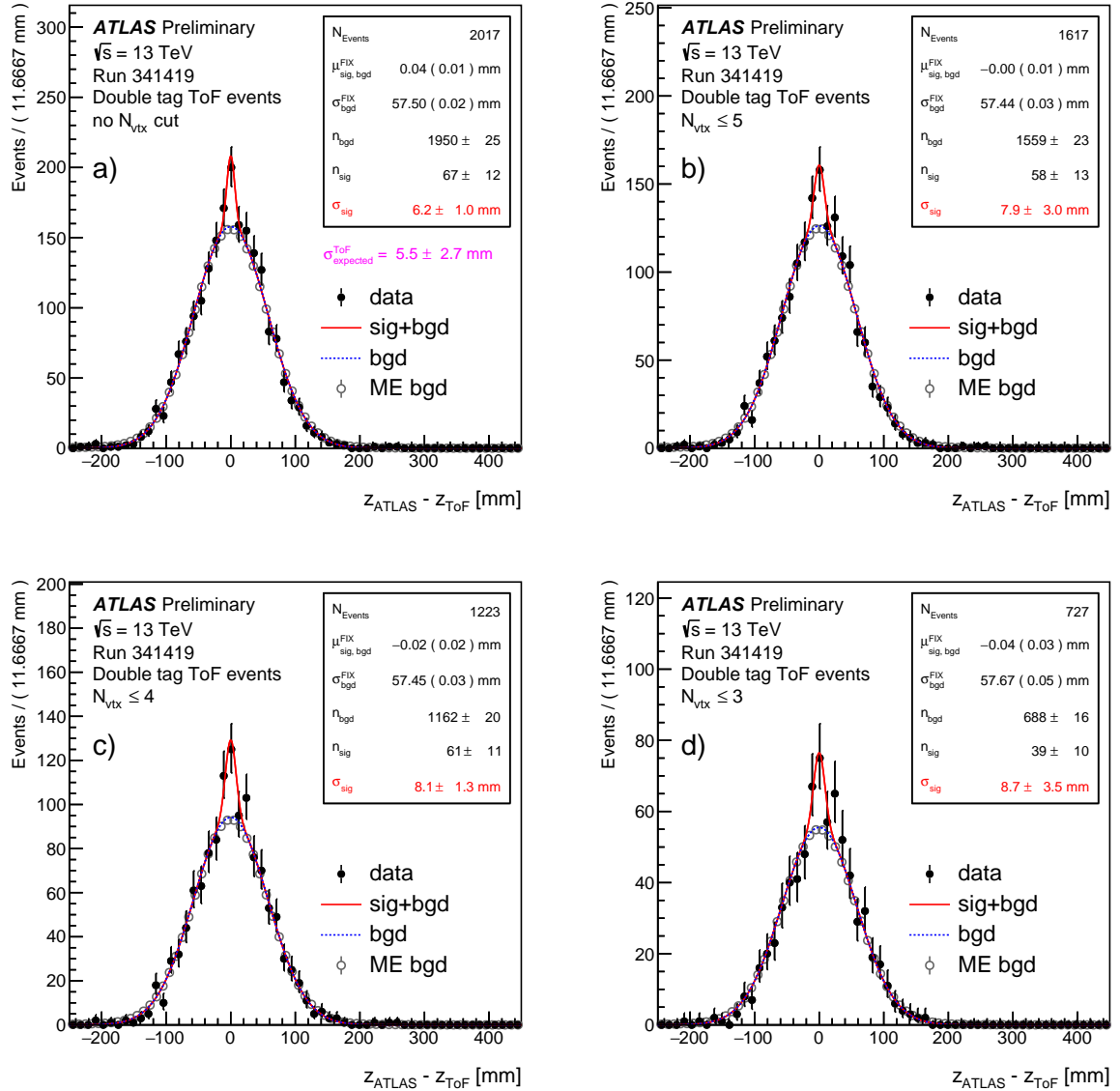Table 8: Signal width and event yield as well as the background event yield extracted in run 341419.

Figure 14: The distributions of $z_{ATLAS} - z_{ToF}$ measured in events with ToF signals on both sides of the interaction region in run 341419, where z_{ATLAS} stands for vertex z-positions reconstructed as primary ones by ATLAS. The distributions shown in figures a)-d) correspond to ATLAS data containing a reconstructed primary vertex together with coincidence of signals in both ToF detectors in four cut scenarios with respect to number of vertices reconstructed by ATLAS, no N_{vtx} cut, $N_{vtx} \leq 5$, $N_{vtx} \leq 4$ and $N_{vtx} \leq 3$, respectively. A double Gaussian function representing the signal and background components is fitted to unbinned data samples using the extended negative log-likelihood fit as implemented in RooFit in all N_{vtx} cut scenarios. The mean of the signal component as well as the mean and width of the background component are always estimated from a Gaussian fit to the mixed event data in each N_{vtx} cut scenario separately, denoted as μ_{sig}^{FIX}, μ_{bgd}^{FIX} and σ_{bgd}^{FIX}. The mixed event data $z_{ATLAS} - z_{ToF}$ distributions are obtained by random mixing of times measured by ToF in either station and the z_{ATLAS} values which do not originate in the same collision event. The expected resolution of the ToF detector, quoted as $\sigma_{expected}^{ToF}$ is obtained from the known single-channel resolutions convoluted with the actual channel-hit-patterns observed in the data in the no N_{vtx} cut scenario.

5 Conclusions

Single channel and train efficiencies are measured in three AFP calibration stream runs from 2017. Average train efficiencies between 6% to 9% and 3% to 5% are observed in the FAR-A and FAR-C station in low μ run 331020, respectively. The efficiencies drop to about 5% in FAR-A and $2 - 3$% level in FAR-C station, respectively, in the low μ run 336505 recorded two months after the run 331020. From the high μ run 336506 taken immediately after the run 336505 it can be deduced that the efficiency is insensitive to the rate of incoming protons, which is proportional to μ. The low and continuously decreasing efficiencies measured in the single channels and the trains are caused by low signal amplitudes at the output of the PMTs caused by the exceeded lifetimes of the PMTs.

The resolutions of individual ToF channels are extracted using the method of time differences measured between channels in single trains. The analysis of widths of the time difference distributions yields single channel resolutions with typical magnitude of 40, 30, 20, 30 ps for channels corresponding to bars A,B,C,D. The least performing channels in terms of resolution correspond to first LQ-bars (A) of the trains. In turn, the next bars in the train profit from photon statistics enrichment from the preceding bars, leading to a stronger signal and a better time resolution. No significant change is observed between the resolutions measured in the early run 331020 and the later run 336505. The total uncertainty reaching up to 6 ps in some channels is dominated by systematic effects.

The resolution of the z-coordinate of the primary vertex reconstructed by the ToF, z_{ToF}, is estimated by a comparison with the value of primary vertex z position provided by ATLAS, z_{ATLAS}, in the run 341419. The data indicate there is a signal contribution observed as an excess above the combinatorial background in the $z_{\text{ATLAS}} - z_{\text{ToF}}$ distribution. The parameters of the signal contribution are extracted from fits. The signal widths, directly related to the ToF resolution, are measured of about 6.2 ± 1.0 mm to 8.5 ± 3.4 mm depending on the statistics of the fitted data obtained in several cut scenarios with respect to number of vertices reconstructed by ATLAS. The results are within uncertainties consistent with the expected resolution of the ToF system of 5.5 ± 2.7 mm, estimated mainly from a detailed study of single-channel resolutions.

References

[1] L. Adamczyk et al., *AFP: A Proposal to Install Proton Detectors at 220,m around ATLAS to Complement the ATLAS High Luminosity Physics Program*, tech. rep. ATL-COM-LUM-2011-006, AFP technical proposal: CERN, 2011, URL: https://cds.cern.ch/record/1331213 (cit. on p. 2).

[2] J. Lange et al., *Beam tests of an integrated prototype of the ATLAS Forward Proton detector*, Journal of Instrumentation **11** (2016) P09005, URL: http://stacks.iop.org/1748-0221/11/i=09/a=P09005 (cit. on p. 2).

[3] *Suprasil UVL datasheet*, Heraeus, 2018, URL: https://www.heraeus.com/media/media/hqs/doc_hqs/products_and_solutions_8/optics/Suprasil_UVL_synthetic_fused_silica_EN.pdf (cit. on p. 2).

[4] L. Nozka, A. Brandt, M. Rijssenbeek, T. Sykora, T. Hoffman, J. Griffiths, J. Steffens, P. Hamal, L. Chytka, and M. Hrabovsky, *Design of Cherenkov bars for the optical part of the time-of-flight detector in Geant4*, Optics Express **22** (2014) 28984 (cit. on p. 2).

[5] L. Nozka et al., *Design of Cherenkov bars for the optical part of the time-of-flight detector in Geant4*, Opt. Express **22** (2014) 28984 (cit. on p. 2).

[6] *miniPLANACON XPM85112*, PHOTONIS USA Pensylvania Inc., 2014, URL: https://www.photonis.com/uploads/datasheet/pd/Mini-PLANACON-4x4-datasheet.pdf (cit. on p. 3).

[7] M. Rijssenbeek, 'ATLAS Forward Proton Detectors: Time-of-Flight Electronics', *Proceedings of Workshop on Picosecond Photon Sensors for Physics and Medical Applications, Clermont-Ferrand, France, March 12–14, 2014, Acta Phys. Pol. B Proc. Suppl.* Vol. 7, 2014 751 (cit. on p. 3).

[8] M. Mota et al., 'A flexible multi-channel high-resolution time-to-digital converter ASIC', *2000 IEEE Nuclear Science Symposium. Conference Record (Cat. No.00CH37149)*, vol. 2, 2000 9/155 (cit. on p. 3).

[9] L. Chytka et al., *Timing resolution studies of the optical part of the AFP Time-of-flight detector*, Opt. Express **26** (2018) 8028, URL: http://www.opticsexpress.org/abstract.cfm?URI=oe-26-7-8028 (cit. on p. 10).

[10] W. Verkerke and D. P. Kirkby, *The RooFit toolkit for data modeling*, eConf **C0303241** (2003) MOLT007, [,186(2003)], arXiv: physics/0306116 [physics] (cit. on p. 16).

[11] R. Brun and F. Rademakers, 'ROOT - An Object Oriented Data Analysis Framework', *Proceedings AIHENP'96 Workshop, Lausanne, Nucl. Inst. and Meth. in Phys. Res.* Vol. A, 389, 1997 81, URL: http://root.cern.ch/ (cit. on p. 16).

[12] E. Feinberg and I. Pomerančuk, *High-energy inelastic diffraction phenomena*, Nuovo Cim. Suppl. **3** (1956) 652 (cit. on p. 18).

[13] G. Ingelman and P. Schlein, *Jet structure in high mass diffractive scattering*, Physics Letters B **152** (1985) 256, ISSN: 0370-2693, URL: http://www.sciencedirect.com/science/article/pii/0370269385911815 (cit. on p. 18).

[14] T. Aaltonen et al., *Diffractive Dijet Production in $\bar{p}p$ Collisions at $\sqrt{s}$ = 1.96 TeV*, Phys. Rev. D **86** (2012) 032009, arXiv: 1206.3955 [hep-ex] (cit. on p. 18).